

Article

Subscriber access provided by UNIV OF WISCONSIN - MADISON

## Optically detected magnetic resonance for selective imaging of diamond nanoparticles

Margaret E Robinson, James D Ng, Huilong Zhang, Joseph T. Buchman, Olga A. Shenderova, Christy L. Haynes, Zhenqiang Ma, Randall H. Goldsmith, and Robert J Hamers

Anal. Chem., Just Accepted Manuscript • DOI: 10.1021/acs.analchem.7b03157 • Publication Date (Web): 13 Nov 2017

Downloaded from http://pubs.acs.org on November 14, 2017

#### **Just Accepted**

"Just Accepted" manuscripts have been peer-reviewed and accepted for publication. They are posted online prior to technical editing, formatting for publication and author proofing. The American Chemical Society provides "Just Accepted" as a free service to the research community to expedite the dissemination of scientific material as soon as possible after acceptance. "Just Accepted" manuscripts appear in full in PDF format accompanied by an HTML abstract. "Just Accepted" manuscripts have been fully peer reviewed, but should not be considered the official version of record. They are accessible to all readers and citable by the Digital Object Identifier (DOI®). "Just Accepted" is an optional service offered to authors. Therefore, the "Just Accepted" Web site may not include all articles that will be published in the journal. After a manuscript is technically edited and formatted, it will be removed from the "Just Accepted" Web site and published as an ASAP article. Note that technical editing may introduce minor changes to the manuscript text and/or graphics which could affect content, and all legal disclaimers and ethical guidelines that apply to the journal pertain. ACS cannot be held responsible for errors or consequences arising from the use of information contained in these "Just Accepted" manuscripts.



# Optically detected magnetic resonance for selective imaging of diamond nanoparticles

Margaret E. Robinson<sup>†</sup>, James D.  $Ng^{\dagger}$ , Huilong Zhang<sup>‡</sup>, Joseph T. Buchman<sup>§</sup>, Olga A. Shenderova, \*\*Christy L. Haynes<sup>§</sup>, Zhenqiang Ma<sup>‡</sup>, Randall H. Goldsmith<sup>†</sup>, and Robert J. Hamers<sup>†\*</sup>

<sup>†</sup>Department of Chemistry, University of Wisconsin-Madison, 1101 University Avenue, Madison, WI 53706, United States

\*Adámas Nanotechnologies, 8100 Brownleigh Dr, Raleigh, NC 27617

<sup>‡</sup>Department of Electrical and Computer Engineering, University of Wisconsin-Madison, 3445 Engineering Hall, 1415 Engineering Drive, Madison, Wisconsin 53706

<sup>§</sup>Department of Chemistry, University of Minnesota, 207 Pleasant St SE, Minneapolis, MN 55455, United States

**ABSTRACT:** While there is great interest in understanding the fate and transport of nanomaterials in the environment and in biological systems, the detection of nanomaterials in complex matrices by fluorescence methods is complicated by photodegradation, blinking, and by the presence of natural organic material and other fluorescent background signals that hamper detection of fluorescent nanomaterials of interest. Optically detected magnetic resonance (ODMR) of nitrogen-vacancy ( $N_V$ ) centers in diamond nanoparticles provides a pathway toward background-free fluorescence measurements, as the application of a resonant microwave field can selectively modulate the intensity from  $N_V$  centers in the diamond in nanodiamonds of various diameters in complex materials systems using on-resonance and off-resonance microwave fields. This work represents the first investigation showing how nanoparticle diameter impacts the  $N_V$  center lifetime and thereby directly impacts the accessible contrast and signal-to-noise ratio when using ODMR to achieve background-free imaging of  $N_V$  nanodiamonds in the presence of interfering fluorophores. These results provide new insights that will guide the choice of optimum nanoparticle size and methodology for background-free imaging and sensing applications, while also providing a model system to explore the fate and transport of nanomaterials in the environment.

One of the key challenges of analytical chemistry is to selectively identify individual species within complex systems. An emerging problem of particular significance and difficulty is to understand the fate and transport of nanomaterials in environmental and biological systems.1-6 While the last decade has witnessed outstanding progress in the development of single-photon and sub-diffraction optical methods,<sup>7-9</sup> the use of fluorescence methods to characterize nanomaterials is hampered by the fact that most fluorescent nanoparticles are unstable over the extended time course (frequently days to weeks) associated with biological exposure studies,10-13 and complex background signals associated with environmental matrices frequently interfere with emission from nanoparticles of interest.14,15 Organic chromophores can be grafted onto nanoparticle surfaces, but can be chemically ligated by enzymes and other molecules, are subject to bleaching under intense illumination, and can exhibit cytotoxicity.16 Consequently, there remains an unmet need for highly stable and selective fluorescent nanoparticles that are non-toxic and will not degrade over extended times in environmental and/or biological media, even under intense illumination.<sup>17,18</sup> A particularly acute challenge in environmental systems is to distinguish fluorescence of the fluorophore probe from competing optical signals such as scattering and autofluorescence.<sup>19</sup>

Diamond nanoparticles containing N<sub>V</sub> centers have recently emerged as a nanomaterial of great potential interest for biological and environmental imaging. 20-22 N<sub>V</sub> centers consist of a substitutional N atom with an adjacent vacancy, forming a highly stable, non-bleachable solidstate fluorophore that exists in neutral (N<sub>V</sub><sup>o</sup>) and negative  $(N_V)$  charge states.  $N_V$  centers can be excited using easily accessible visible wavelengths and emit at wavelengths of 638-800 nm, a region well-suited to imaging in biological samples. 23,24 Furthermore, the high chemical stability and ability to covalently functionalize the surface of diamond provides a pathway to tailor the surface properties of N<sub>V</sub> nanodiamonds in a flexible and highly stable manner. 25-27 The negatively charged  $N_V$  center,  $N_V$  is a particularly novel fluorophore because its fluorescence intensity is sensitive to the presence of magnetic fields<sup>28</sup> and can be modulated by resonant excitation with a weak microwave excitation,<sup>29</sup> a technique known as optically detected magnetic resonance (ODMR).30 ODMR is enabled by the fact that the N<sub>V</sub> defect is a triplet spin system with magnetic sublevels separated by microwave frequencies, and by relaxation dynamics that make the intensity of N<sub>V</sub> fluorescence sensitive to the distribution of spins into these sublevels. ODMR is important for imaging applications because it provides a way to selectively modulate the intensity of N<sub>V</sub>-containing nanodiamonds using relatively weak microwave fields, while the vast majority of other fluorescent moieties remain unaffected by the microwaves. Thus, ODMR provides a way to selectively identify fluorescence from diamond nanoparticles in the presence of autofluorescence, scattering, and other spectrally overlapped background signals.<sup>28,31</sup> In addition to imaging in biological systems,<sup>29,32,33</sup> ODMR can also be used in principle as a probe of local magnetic fields,<sup>34-38</sup> electric fields,<sup>39</sup> spin,<sup>40</sup> and temperature.<sup>41</sup> Thus, ODMR in nanodiamond has great potential as a quantum-based analytical tool for addressing a wide range of analytical sensing and selective imaging problems..

Although the properties of  $N_V$  centers have been widely studied in bulk diamond, <sup>42</sup> the factors controlling the use of ODMR to achieve selective imaging of nanodiamonds in the presence of background emitters remain poorly understood. <sup>43-47</sup> Of particular importance is that while the charge state and dynamics of  $N_V$  centers have been shown known to depend on nanoparticle size, <sup>48-52</sup> the manner in which nanoparticle size influences the underlying dynamics and the resulting contrast and signal-to-noise ratio of ODMR for selective imaging in environmental and biological systems has not been established previously.

Here, we present studies of the critical factors controlling the ability to selectively image N<sub>V</sub> nanodiamond in the presence of other fluorescent moieties using optically detected magnetic resonance (ODMR) in a full-frame imaging configuration and in spectroscopic mode, using N<sub>V</sub>-containing nanodiamonds of different sizes derived from the same starting material and thereby having a constant density of N<sub>V</sub> centers. We demonstrate selective imaging of N<sub>V</sub> nanodiamonds down to 40 nm diameter by direct digital subtraction of full-frame images acquired with a weak microwave field alternatively applied offresonance and on-resonance. Full-frame imaging and spectroscopically resolved data using nanodiamonds of different sizes derived from a common starting material (thereby ensuring constant N<sub>V</sub> concentration) show that the selectivity associated with ODMR imaging decreases for small nanodiamonds due both to a shift in the  $N_{\rm V}$ charge state from the negatively charged N<sub>V</sub> center to the neutral N<sub>V</sub>° center and because of non-radiative relaxation processes associated with the nanodiamond surfaces. Our results highlight the important physical processes and imaging conditions that control the signal-to-noise ratio associated with the use of ODMR to achieve selective imaging of nanodiamond in the presence of background signals such as non-diamond fluorescence and/or scattering. These insights will inform the use of N<sub>V</sub> containing nanodiamonds in background-free imaging and guide the understanding of how to use the unique magnetic resonance properties of N<sub>V</sub> nanodiamond to enable new approaches to background-free, selective imaging of nanomaterials in complex matrices.

#### **Experimental Section:**

Nanoparticles. Suspensions of oxidized, size-selected (0.1% by weight) nanodiamond with enhanced concentrations of N<sub>V</sub> centers were provided by Adámas Nanotechnologies (Raleigh, NC) with nominal diameters ranging from 10 nm to 100 nm. 15-µm-diameter N<sub>V</sub>-implanted diamond powder was also provided. N<sub>V</sub> centers were produced by irradiating 15 µm and 100 nm particles with 2 MeV electrons to a dose of 5x10<sup>18</sup> e<sup>-</sup>/cm<sup>2</sup> followed by annealing at 850°C for 2 hrs and cooling to room temperature. Nanoparticles with 10, 20, 30, 40, and 60 nm diameters were made by mechanically fracturing the larger 15 µm diameter material after activation and annealing. The micron-size particles were milled in a planetary mill using ceramic 1 cm diameter balls, purified from milling media in HF and HNO3 acids, washed with deionized water and fractionated into smaller sizes in deionized water media using an ultracentrifuge with up to 45,000 RCF for 4 hrs for the smallest 10 nm particles. Since Nv centers were formed in the 15 mm diamond before fracturing into smaller sizes, our procedure ensures that nanoparticle of all sizes have the same total concentration of N<sub>V</sub> centers, distributed between the two charge states  $N_V^{o}$  and  $N_V^{-}$ . The 100 nm particles were processed separately by the same method. The total substitutional nitrogen content (N<sub>s</sub>) in 15 µm and 100 nm starting material was determined to be ~100-120 ppm as measured by electron paramagnetic resonance (EPR).<sup>53</sup> The concentration of negatively charged  $N_V$  centers was also determined by EPR for each size, yielding values of 4 ppm for 15 μm, 2.5 ppm for 100 nm, 1.5ppm for 60 nm and below 1 ppm for 10, 20, 30, and 40 nm diameter particles, correspondingly. Detailed procedures for the ESR measurements are in the SI. Each nanodiamond sample was characterized by dynamic light scattering (Malvern Zetasizer Nano ZS) and by transmission electron microscopy (TEM) to assess particle size and distribution (see SI).

**Measurement of emission spectra.** Spectra were measured using the apparatus depicted in Fig. 1. Emission spectra were collected using a 532 nm continuous-wave diode pumped solid-state laser (Opto Engine LLC, MLL-FN-532-500m) typically using 100 mW focused onto the

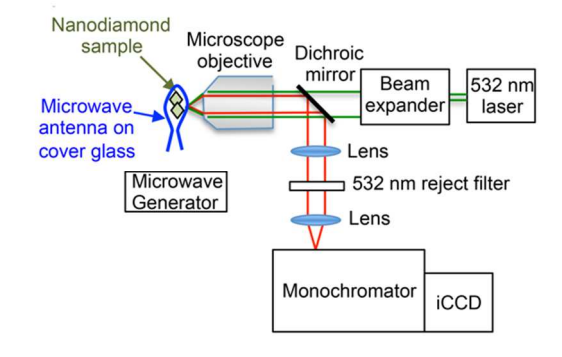


Figure 1: Optical apparatus for performing emission spectra, imaging, and optically detected magnetic resonance experiments.

sample using a 40x microscope objective. The fluorescence was collected using the same lens, filtered using a dichroic mirror (Semrock, FF553-SDio1-25x36) and a 532 nm line-reject filter (Semrock, NF01-532U-25) and focused into the 25 µm slit of an Andor Shamrock 193i monochromator with a grating blazed at 760 nm and 150 lines/mm. The detector was an Andor iStar intensified CCD (DH334T-18F-03). All spectra presented here were calibrated using the 532 nm laser line. For optical measurements, a small aliquot of 10 µL of nanodiamond solution was dried onto a cover glass. A consistent procedure was followed for deposition of the nanodiamonds using dispersions of similar same mass concentration; consequently, the mass density of nanoparticles and the area density of N<sub>V</sub> centers are expected to be similar between different samples.

**Microwave modulation.** A 50-Ω-impendence-matched antenna was fabricated on top of the cover glass using photolithography and metal lift-off processes. This antenna, described previously,<sup>54</sup> consists of a circular loop approximately 1 mm in diameter. Microwaves were generated by an Agilent E8251A PSG-A series microwave source and amplified by a power amplifier (ZVE-3W-83+ from Minicircuits) with a power gain of 35 dB and a saturated power of 35 dBm. Experiments reported here used 16 dBm output power from the source, before amplification.

Differential imaging with microwave modulation. Differential imaging was performed using the apparatus shown in Fig 1a with a 20x microscope objective. Images of the same location were collected using 2.87 GHz (onresonance) and 2.93 GHz (off-resonance) microwave frequencies. Images were registered and digitally subtracted (off resonance – on resonance) to yield a differential image of where the fluorescence intensity of the  $N_{\rm V}$  centers have been modulated by the resonant microwave field.

Fluorescence lifetime measurements. Fluorescence lifetime measurements were collected using a 3-ns, 20 Hz repetition rate 532 nm Nd:YAG-laser (Ekspla, NT 342B-SH-20-AW) to excite nanodiamonds dried onto a CaF<sub>2</sub> disc using a 5x microscope objective; the fluorescence was collected using the same lens, filtered using a dichroic mirror (Semrock, FF553-SDio1-25x36) and a 532 nm line reject filter (Semrock, NF01-532U-25). Fluorescence was collected using a biased Si photodiode (Thorlabs, DET025A) and recorded on an oscilloscope (Agilent Technologies, DSO9404A, 4 GHz). The resulting fluorescence time traces were fit to a single exponential decay.

#### **Results:**

Emission and Optically Detected Magnetic Resonance from nanodiamond samples: Fig. 2a shows typical emission spectra obtained from nanodiamond samples of different diameters. The negatively charged  $N_{\rm V}$  center emits with a zero-phonon line at 637 nm and a broad phonon sideband extending to nearly 750 nm; the neutral  $N_{\rm V}{}^{\rm o}$  charge state has a zero-phonon line at 575 nm and a sideband to longer wavelengths that overlaps with emission from the  $N_{\rm V}{}^{\rm o}$  state. These spectra are similar to those reported previously, exhibiting increased emission from

the neutral  $N_V^{\,\circ}$  center as nanodiamond size decreases.<sup>47</sup> The spectra reported here were individually normalized to demonstrate the changes in spectral distribution. The smaller nanodiamonds also show weaker emission overall. At the smallest sizes the emission spectrum exhibits additional features near 550-570 nm arising from Raman scattering from diamond and non-diamond carbon. These features appear more apparent for small-size nanodiamond because the  $N_V^{\,\circ}$  emission is weaker.

Based on the spectra in Figure 2a, we selected nanodiamonds for further investigation by optically detected microwave resonance (ODMR).<sup>30</sup> Figure 2b depicts the overall scheme of resonant-microwave-induced ODMR. ODMR involves three phenomena: (1) optical spin-pumping preferentially pumps spins into a specific magnetic sub-level ( $m_s$ =0) of the ground electronic state; (2) the intensity of emitted fluorescence depends on the distribution of spins, with  $|e,|m_s$ =0>  $\rightarrow$   $|g,m_s$ =0> transitions more intense than  $|e,m_s$ =  $\pm$  1>  $|g,m_s$ =  $\pm$  1> transitions;

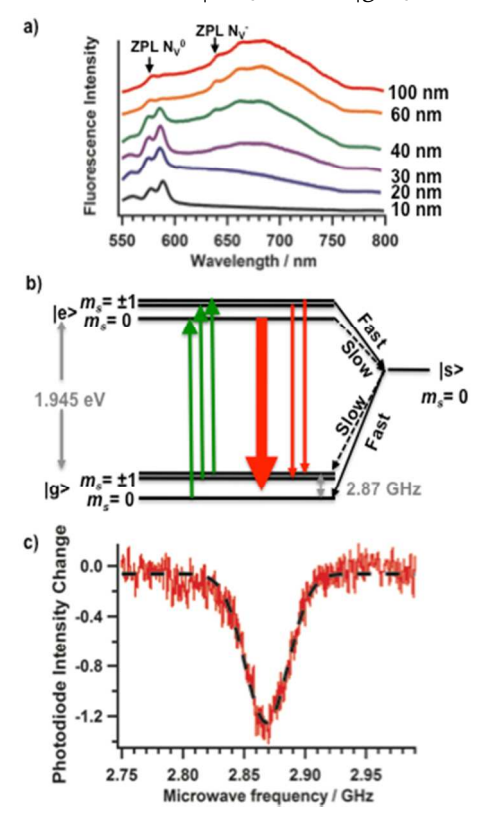


Figure 2: a) Nanodiamond size-dependent emission of  $N_V$  centers with zero phonon lines (ZPLs) of the neutral and negative charge states b) Schematic illustration of ODMR, where  $|g\rangle$  is the electronic ground state,  $|e\rangle$  is the electronic excited state, and  $|s\rangle$  is a metastable singlet state. The  $|g\rangle$  to  $|e\rangle$  transition has a zero-phonon line at 637 nm c) Microwave frequency-dependent photoluminescence emission on 100 nm nanodiamond. The decrease in emission intensity at 2.87 GHz corresponds to resonant excitation of the spins.

and (3) excitation with microwaves at the resonance fre-

1

quency redistributes the spin population among the magnetic sublevels, thereby altering the intensity of fluorescence.

In ODMR, a continuous-wave excitation at 532 nm excites spins from the ground electronic state  $|g\rangle$  (=  ${}^{3}A_{2}$ ) to the first excited electronic state |e> (= 3E). Prior studies have shown that the optical transition dipoles are identical for all three magnetic sublevels.<sup>55</sup> However, intersystem crossing to a dark singlet state occurs faster for the  $|e,m_s=\pm 1\rangle$  states than for the  $|e,m_s=0\rangle$  sublevel. Consequently, the intensity of emission from the |e,m<sub>s</sub>=o> sublevel is greater than that from the  $|e,m_s=\pm 1\rangle$  sublevels. At sufficiently high excitation intensity, repeated excitation-relaxation cycles leads to depletion of the |g,m<sub>s</sub>=±1> sublevels and pumps spins into the |g,m<sub>s</sub>=o> sublevel. The N<sub>V</sub> center has a zero-field splitting between the  $|g,m_s=o\rangle$  to  $|g,m_s=\pm i\rangle$  sublevels, but the  $|g,m_s=\pm i\rangle$  and |g,m<sub>s</sub>=-1> levels are degenerate in the absence of a magnetic field (as in all experiments reported here). If a strong microwave field at a frequency v is applied whose energy, hy, matches the energy difference between the  $|g,m_s=0\rangle$  and  $m_s=\pm 1\rangle$  levels, then the population of the magnetic sublevels will be equalized. This equalization decreases the population of spins in the |g, m<sub>s</sub>=o> state and consequently reduces the total intensity of fluorescence emitted by the N<sub>V</sub> center.

Fig. 2c shows a swept-frequency ODMR experiment on 100 nm  $N_V$ -nanodiamond. In this case, an avalanche photodiode (PicoQuant,  $\tau$ -spad) was used to collect and detect fluorescence. The GHz-frequency microwave signal was amplitude-modulated at 200 Hz and a lock-in amplifier (Signal Recovery 7265) was used to record the synchronized 200 Hz modulation in the detector output as the microwave frequency was swept across the  $N_V$  center resonance. Figure 2b shows the output of the lock-in amplifier as a function of microwave frequency. The fluorescence intensity decreased near 2.87 GHz due to the ODMR process. Fitting the observed dip to a Gaussian function yields at 2.868 GHz center frequency and a standard deviation of 18 MHz, shown by the dashed line.

The emission spectra in Fig. 2a show that small-diameter nanodiamonds exhibit emission from  $N_{\rm V}{}^{\rm o}$  and Raman scattering in addition to  $N_{\rm V}{}^{\rm o}$  emission. To determine how the ODMR contrast varies with wavelength, we used the monochromator and CCD array to measure the emission spectra from ensembles of diamond nanoparticles, with spectra acquired while applying on-resonance (2.87 GHz) and then off-resonance (2.80 GHz) microwave fields. We then determined the effective wavelength-dependent contrast at each wavelength as

$$ODMR\;Contrast(\lambda) = 100 \times \frac{{\scriptstyle N_{off-resonance}(\lambda) - N_{on-resonance}(\lambda)}}{{\scriptstyle N_{off-resonance}(\lambda)}}$$

Fig. 3 shows the effective ODMR contrast for each sample. At short wavelengths the contrast from all samples is reduced because of additional emission from  $N_{\rm V}{}^{\rm o}$  and Raman scattering at these wavelengths. For all samples, the emission reaches a plateau at wavelengths >650 nm. The existence of this plateau indicates that for emission wavelengths >650 nm, emission from  $N_{\rm V}{}^{\rm o}$  is the only sig-

nificant emission source. The existence of a size-dependent plateau shows that the decrease in efficiency as a function of size cannot be accounted for by the changes in emission spectrum distribution alone, since at long wavelengths where only  $N_{\rm V}^-$  emits the contrast remains size-dependent.

Optically Detected Magnetic Resonance Imaging. To demonstrate the ability to use ODMR in an imaging mode to selectively image fluorescence from  $N_V$  nanodiamond in the presence of non-diamond fluorescent emitters, we characterized samples made by depositing both  $N_V$  nanodiamonds and  $Al_2O_3{:}Cr^{3^+}$  (ruby) particles onto microscope cover-slips, adjusting the amounts

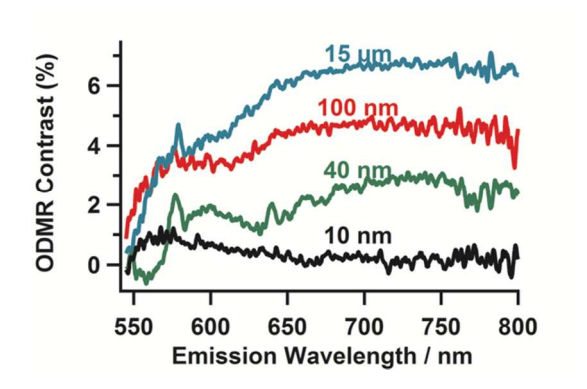


Figure 3: Wavelength-dependent ODMR contrast for nanodiamonds of selected sizes. On-resonance frequency=2.87 GHz; off-resonance frequency =2.80 GHz.

deposited to yield similar fluorescence intensities. In tests shown here, we deposited nanodiamond and nanoruby from aqueous suspension into separate regions separated by a barrier layer made from a silicone polymer. In this way both fluorescent materials were located within the optical system's field of view at the same time, facilitating quantitative analysis of relevant imaging characteristics. Ruby particles were used in these tests because ruby's fluorescence spectrum, consisting of two sharp peaks near 700 nm with phonon sidebands extending from ~670 nm to 730 nm (shown in Supporting Information) is spectrally overlapped with that of nanodiamond and does not bleach, providing a reproducible, spectrally overlapped comparison sample for testing purposes. In these experiments, the detection optics included only a 532 nm notch filter to reject laser scatter; all other emission wavelengths, including emission from N<sub>V</sub> nanodiamond, ruby, and Raman scattering were collected.

Figure 4 shows a series of raw and processed images from 100 nm, 40 nm, and 10 nm nanodiamond. The top two panels in Fig. 4 show raw grayscale images of regions containing nanodiamonds and ruby particles obtained with microwaves applied off-resonance (2.93 GHz, Fig. 4a, 4f, 4k) and on-resonance (2.87 GHz, Fig. 4b, 4g, 4l) using a conventional grayscale mapping. For each nanodiamond size, the off-resonance and on-resonance images appear nearly identical. However, taking the difference between the images as  $I_{2.93GHz}$ – $I_{2.87GHz}$  yields images (Fig. 4c, 4h,

1

4m) that reflect the spatial variations in microwaveinduced modulation of the fluorescence intensity, which we refer to as the "ODMR difference image." Since difference values can be positive or negative, these data are represented here as a grayscale image with mid-gray representing no modulation, and white regions indicating a decrease in intensity upon application of a resonant microwave field. Thus, under these conditions it is expected that only nanodiamond should exhibit a positive signal, while ruby and other fluorescence chromophores, along with scattered light, should yield signals near zero. To illustrate more quantitatively the signal changes, the fourth row of images (Fig. 4d, 4i, 4n) shows crosssectional line cuts through the ODMR difference images along the dashed orange lines. These cross-sectional images show that in the non-diamond regions the signal fluctuates about zero. These fluctuations in intensity are higher in the region containing ruby compared with those in the region containing the hydrophobic barrier layer, demonstrating that non-ODMR fluorescence signals contribute noise to the differential images.

To achieve a more robust signal-to-noise analysis, we note that for photon-counting systems the signal-to-noise ratio is typically limited by shot noise in the number of counts detected. Thus noise,  $\Delta N_{shot}$ , scales like the absolute number of counts *N* as  $\Delta N_{shot} = \sqrt{N}$ . Here, 10<sup>4</sup><N<10<sup>7</sup> at all points in each image and the absolute differences between on-resonance and off-resonance images are << N. Under these conditions is noise in each pixel of the difference image will scale approximately as  $\Delta N_{shot}$  =  $\sqrt{2N}$ , where the 2 arises from the assumption that the noise in the on-resonance and off-resonance images are uncorrelated with each other. Since the modulation in intensity between off-resonance and on-resonance images is small (a few percent), the shot noise at each pixel is approximately  $\Delta N_{shot} = \sqrt{N_{off-resonance}}$ . The signal-tonoise (S/N) ratio at each pixel for the ODMR experiment can then be predicted to be:

$$\frac{\textit{ODMR Signal}}{\textit{Noise}} = \frac{\textit{N}_{2.93GHz} - \textit{N}_{2.87GHz}}{\sqrt{2\textit{N}_{2.93GHz}}}.$$

This value represents a way to quantitatively assess whether local ODMR difference signals are real or are

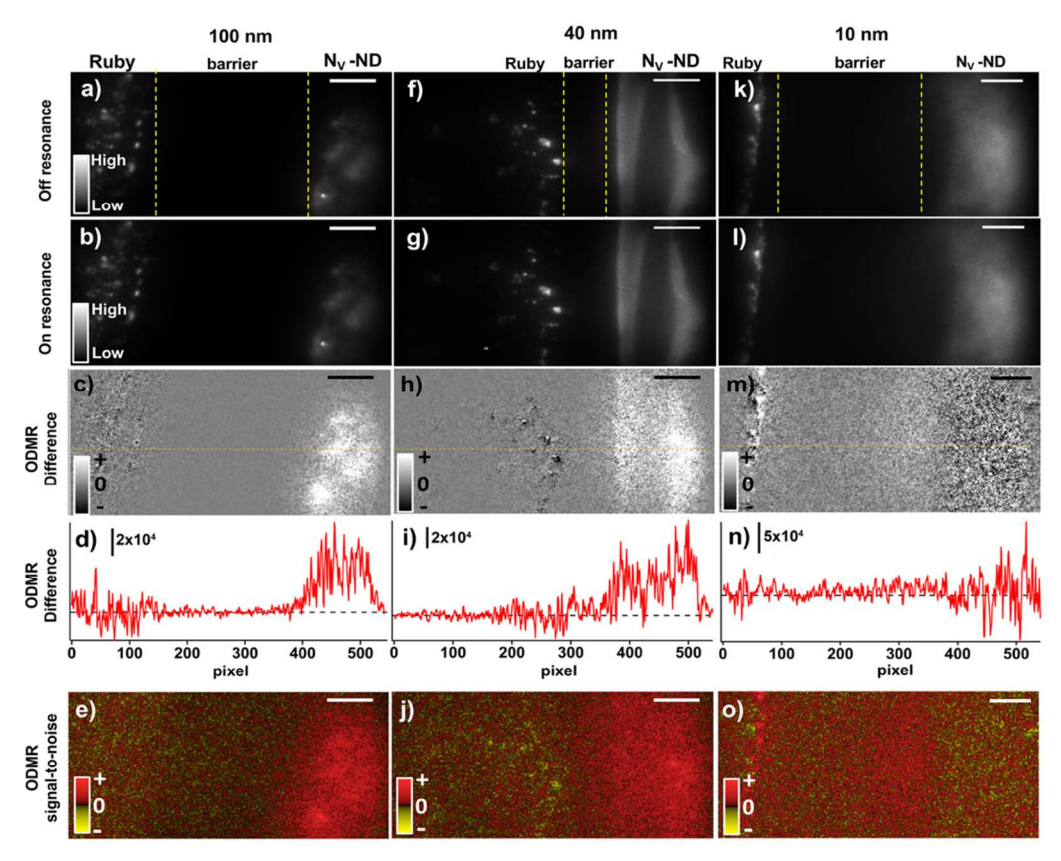


Figure 4: Demonstration of the ability to selectively image nanodiamond using 100 nm (a-e), 40 nm (f-j), and 10 nm (k-o) diameter nanodiamond and ruby particles. Images a, f, and k were collected with an off-resonance, 2.93 GHz, microwave frequency. Images b, g, and l were collected with the on-resonance, 2.87 GHz, microwave frequency. Grayscale ranges are nearly identical for (a,b,f,g,k,l) ranging from zero to  $\sim 6 \times 10^6$  counts per pixel. Images c, h, and m show the difference image  $I_{2.93 \text{GHz}} - I_{2.87 \text{GHz}}$ , representing the microwave-induced modulation in intensity. In this representation nanodiamond should give rise to positive signals, represented as white in the image. Fig. d, I, and n show cross-sections through the ODMR difference images. Finally, Fig. e, j, and o show the ODMR signal-to-noise ratio, as explained in text. Vertical scale ranges are S/N=(-100,100) for e and j, and S/N=(-30,+30) for panel o. Horizontal scale bars are 25  $\mu$ m for all images.

within the noise limits set by counting statistics at each individual pixel. The fifth row in Fig. 4 (Fig. 4e, 4j, 4o) shows such spatial maps of ODMR signal-to-noise. Here we use a color scale to more clearly show both positive and negative values. For the sample containing 100 nm nanodiamond, the signal-to-noise map (Fig. 4e) shows almost uniformly positive signals on the right-hand side of the image where the nanodiamond is located, demonstrating that the ODMR signal is well outside the signalto-noise limits established by counting statistics. In contrast, in the barrier region and in the region containing ruby particles (left side of image) there are small regions of both positive and negative ODMR signal, but no extended spatial regions where the S/N ratio is large and positive. Similarly, for 40 nm nanodiamond the ODMR difference image (Fig. 4h) shows strong modulation in the region where the nanodiamond is located, and the signalto-noise map (Fig. 4i) shows uniformly high S/N ratio where the nanodiamond is located, but values that fluctuate positively and negatively in the barrier layer and the region where the ruby was located. Finally, for the 10 nm diamond, the ODMR difference signal (Fig. 4m) shows only increased noise in the local region, and the S/N map (Fig. 40) shows that there are no extended regions where the signal-to-noise is uniformly positive, suggesting 10 nm particles are unsuitable for imaging. In Fig. 40, a small patch of apparently positive S/N ratio is visible in the region associated with the ruby particles, but further analysis shows that this feature arises from a small shift in the images due to an electromechanical interaction between the microwave antenna and the microscope stage. Note that Fig. 60 is presented on a more sensitive scale compared with Fig. 6e and 6j.

An alternative way to assess the ODMR signal is via the percent contrast. This parameter is useful because it is a direct reflection of the nanodiamond and the optical excitation system, and should be independent of the properties of the optical collection system. We analyzed the images using one region populated by ruby and one region populated by nanodiamond, and calculated the %Contrast as %  $Contrast = 100 \times \left(\frac{N_{2.93GHz} - N_{2.87GHz}}{N_{2.93GHz}}\right)$ , yielding the values shown in Table 1.

Table 1: Imaging-mode ODMR percent contrast values for ruby and  $N_V$  nanodiamond regions. Fluorescence lifetimes for  $N_V$  nanodiamond samples are also shown with standard deviations of the single exponential fits are given for each fluorescence lifetime measurement.

Diameter (nm)	% ODMR O	Contrast Ruby	Fluorescence lifetime / ns
100	3.37 ± 0.12	0.11 ± 0.09	10.00 ± 0.12
40	2.19 ± 0.11	0.37 ± 0.07	5.38 ± 0.14
10	0.40 ± 0.26	0.04 ± 1.13	≤3 ns

For 100 nm and 40 nm diameter nanodiamond the contrast is several percent, which is readily detectable in imaging mode using a high-quality array detector with sufficiently low dark counts. The 10 nm diamond contrast is less than one percent, challenging the signal-to-noise capabilities of the optical detection. As expected, the regions with background from ruby show apparent ODMR contrast values that are very close to zero.

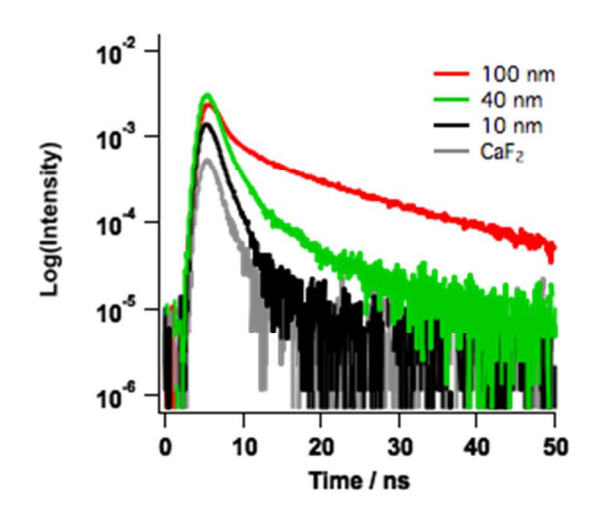


Figure 5: Fluorescence lifetime measurements from  $N_V$  nanodiamonds of different diameters and the reflection of the excitation laser off of the  $CaF_2$  window to show the instrument response function. Vertical axis in arbitrary units.

Fluorescence lifetimes of N<sub>V</sub> centers. The above data indicate that under equivalent imaging conditions, the fractional modulation in intensity associated with application of a microwave field (the "ODMR contrast") is poorer with the smallest-diameter (10 nm) nanodiamond compared with larger (40 nm, 100 nm) nanodiamond. To better understand the origin of these observations, we measured the fluorescence lifetime of the nanodiamond samples using a tunable pulsed laser (~3 ns pulse width) and a fast (2 GHz) photodiode. Figure 5 shows representative fluorescence decay curves from nanodiamond samples of different diameters. Fluorescence lifetimes from samples of different sizes were fit to single-exponents over the 12 ns to 34 ns time interval. As shown in Table 1. the fluorescence lifetime decreases from 10.00  $\pm$  0.12 ns to  $5.38 \pm 0.14$  ns as the nanodiamond size decreases from 100 nm to 40 nm. The lifetime of the 10 nm nanodiamond could not be measured as it indistinguishable from the apparent lifetime of non-fluorescence background signals arising from scattering off the underlying CaF<sub>2</sub> substrate; this indicates the lifetime is shorter than the 3 ns excitation laser pulse. Thus, these data show that the smalldiameter nanoparticles have higher rates of fluorescence decay compared to larger diameter nanoparticles.

These lifetime studies suggest that the reduction in contrast for small-diameter nanodiamonds is likely associated with the presence of additional non-radiative decay pathways that are not spin-selective. Such processes would have the effect of reducing the effectiveness of the spin-pumping and thereby decrease the ODMR contrast. To test whether the contrast could be enhanced for smalldiameter nanodiamond by increasing laser power we conducted a laser power ODMR study. Those experiments (results presented in SI) revealed that the contrast is not significantly enhanced using higher incident laser power. In addition, we observed that higher incident laser powers induce spectral broadening and flatten the zerophonon line of N<sub>V</sub>. These results, in agreement with prior reports by others31, indicate that the loss in contrast for small-diameter nanodiamond cannot be easily rectified by using different conditions of the optical or microwave excitation.

#### **Discussion:**

Our data show that it is possible to selectively image N<sub>V</sub> nanodiamond in the presence of other emitters by using ODMR in an imaging mode by direct subtraction of offresonance and on-resonance images. The ability to selectively image one type of nanoparticle in the presence of other fluorescent moieties has significant potential for use of N<sub>V</sub> nanodiamond as an analytical probe in chemistry and biology. For example, one of the key challenges in understanding the fate, transport, and uptake of nanomaterials in the environment is the difficulty of distinguishing nanoparticle fluorescence from spectrally overlapped signals such as Raman scattering and fluorescence from other species. While our experiments demonstrate that direct ODMR imaging is possible, the ability to achieve this selective imaging decreases significantly as the particle size decreases <40 nm due to reduction in ODMR contrast. This reduction is due to changes in the emission spectrum and a decrease in the lifetime of the N<sub>V</sub> centers. These changes reduce the ODMR contrast from a maximum theoretical value of ~30% reported using high-quality macroscopic diamond samples,56 to lower values of 5% or less for nanodiamonds. While ODMR is in principle "background-free" imaging technique, to effectively use N<sub>V</sub> nanodiamonds in detection systems it is important to address the critical signal-to-noise (S/N) issues that control the ability to selectively identify N<sub>V</sub> nanodiamond from within more complex systems. We consider first the intrinsic S/N properties of the detection system.

The ability to selectively detect ODMR relies on the ability to subtract adjacent images with S/N ratio sufficiently high to distinguish OMDR contrast from noise. In Fig. 4, that background signals other than ODMR are close to zero, but the associated shot noise gives rise to pixel-by-pixel fluctuations. Under the conditions of our experiment (20x magnification, 0.5 numerical aperture objective, f/3.7 monochromator, and 13  $\mu$ m CCD element size), the diffraction-limited Airy disk on the CCD produced by a point source is 6  $\mu$ m diameter, and light emitted from any object <1.5  $\mu$ m diameter is focused onto a single pixel. Detection of *individual*, isolated nanodia-

monds would require sufficient ODMR contrast on individual CCD pixels to exceed the shot noise arising from the background fluorescence, while more spatially extended ensembles of nanodiamonds (as in our experiments, Fig. 4a-4j) can be easily identified by a high S/N ratio that is distributed across many pixels.

The second factor controlling the ability to use ODMR imaging is the size-dependent changes in the nanodiamond spectrum and dynamics. There are two primary contributors to these changes: (1) shifting of the charge state from  $N_V$  to  $N_V$  at small sizes and (2) introduction of new relaxation pathways. These phenomena are both associated with the diamond surfaces. Prior studies have shown that changes in the electrostatic potential at nanodiamond surfaces induce a shift in the charge state of the  $N_V$  center to favor the neutral  $N_V$  center. 46-48 This shift is evidenced in Fig. 2a as increased emission near 630 nm for nanodiamonds that are ~40 nm and below in diameter. While this change in charge state decreases the ODMR contrast when emission is integrated over all wavelengths (as in Table 1), it should not affect the contrast at long wavelengths (e.g., 700-800 nm) where the only emission is from N<sub>V</sub>. However, Fig. 3 shows that the ODMR contrast is reduced even at long wavelengths, implying that other size-dependent factors also are important. The ability to achieve ODMR contrast is strongly dependent on the relative rates of fluorescence and spindependent intersystem crossing. Fig. 5 shows that as the nanoparticle size decreases below 100 nm the lifetime decreases, becoming <3 ns for 10 nm nanodiamond. As a consequence, the overall quantum efficiency for luminescence decreases and other optical processes such as Raman scattering become more apparent when emission spectra are normalized to similar intensities. Thus, the appearance of Raman peaks at 500-600 nm for nanoparticles <40 nm diameter is due in part to the reduced intensity from  $N_V$  emission.

The size-dependent changes in spectral distribution and radiative lifetime both highlight the important role of the nanoparticle surfaces and surface defects that facilitate non-radiative relaxations. If the rates of these non-radiative processes are comparable to or greater than that of relaxation through the single spin system, then the effectiveness of the spin pumping is reduced, leading to reduced ODMR contrast. Attempts to compensate for the reduced pumping efficiency by increasing the incident laser fluence resulted in broadening of the lines and did not significantly increase the contrast, likely due to heating effects.

These results provide a guide for understanding the optimum choice of  $N_V$  nanodiamond for different types of imaging and sensing applications. Our results using nanodiamonds with oxidized surfaces, suggest that 40 nm diameter provides a balance between ODMR contrast and  $N_V$  emission. It is possible that further improvements might be achievable by using nanoparticles with different surface terminations to maintain more  $N_V$  centers in the negative charge state ( $N_V$ ) and by applying surface treatments that reduce the number of mid-gap defect states.

Ultimately the enhanced understanding of sizedependent N<sub>V</sub> dynamics obtained in these studies will be important in the future development of even more advanced imaging techniques that seek to use the N<sub>V</sub> center's long coherence time and other quantum-based properties to achieve new imaging modalities.34-41,54

#### Conclusions:

By modulating the frequency of an applied microwave field, optically detected magnetic resonance induces selective modulation of the intensity of fluorescence emission from N<sub>V</sub> nanodiamond. We have shown that by using differential imaging methods in which images are acquired with the microwave field on-resonance and off-resonance and then subtracted, the N<sub>V</sub> nanodiamond can be selectively imaged in the presence of other fluorophores. The use of very small N<sub>V</sub> nanodiamond for imaging applications is limited by surface states that alter than nanodiamond charge state and reduce the efficiency of optical spin pumping. As the ODMR contrast decreases to below ~2%, effective use of ODMR to selectively identify N<sub>V</sub> nanodiamond in complex matrices may require more elaborate differencing techniques than the direct subtraction method applied here and/or improved control over the nanodiamond surfaces to reduce the effects of surface states. However, for nanodiamonds with diameters as small as 40 nm, an ODMR contrast of several percent is well outside the noise limits of most modern imaging systems and will enable new selective imaging modalities based on the charge and spin properties of N<sub>V</sub> centers.

#### ASSOCIATED CONTENT

#### **Supporting Information**

Emission spectra of detonation nanodiamond and monocrystalline. Emission spectra of 100 nm N<sub>V</sub> nanodiamond using various excitation laser powers. ODMR response of 100 nm  $N_V$  nanodiamond at 100 mW and 500 mW excitation laser powers. TEM images and DLS characterization of nanodiamond samples. This material is available free of charge via the Internet at http://pubs.acs.org.

#### **AUTHOR INFORMATION**

#### Corresponding Author

\*Email: rjhamers@wisc.edu Phone (work): 608-262-6371, Fax: 608-262-0453

#### **Author Contributions**

The manuscript was written through contributions of all authors. All authors have given approval to the final version of the manuscript.

#### **ACKNOWLEDGMENT**

This work was supported by the National Science Foundation via the Centers for Chemical Innovation Program Award CHE-1503408. J.T.B. was supported by the University of Minnesota Biotechnology Training Grant Program through the National Institutes of Health. Fabrication of microwave antennas was supported by Office of Naval Research grant # Noo014-13-1-0226 to Z.Q.M. TEM work in this study was carried out in the Characterization Facility, University of Min-

nesota, which receives partial support from NSF through the MRSEC program. R.H.G. and J.N. acknowledge support from the National Science Foundation via CHE-1254936 for initial studies of N<sub>V</sub>resonance phenomena. N<sub>V</sub> nanodiamond samples were produced by Adamas Nanotechnologies using support from the National Heart, Lung, and Blood Institute, National Institutes of Health (NIHLBI), under Contract No. HHSN268201500010. The authors acknowledge F.J. Heremans and D.D. Awschalom for helpful conversations, C. N. Nunn of Adámas for help with sample preparation and A. Shames of Ben-Gurion University of Negev for providing EPR data on N<sub>V</sub> center content in the samples.

#### **REFERENCES**

- (1) Szakal, C.; Ugelow, M. S.; Gorham, J. M.; Konicek, A. R.; Holbrook, R. D. Anal. Chem. 2014, 86, 3517-3524.
- (2) Hayden, O.; Payne, C. K. Angew. Chem. Int. Ed. 2005, 44,
- (3) Huynh, K. A.; Siska, E.; Heithmar, E.; Tadjiki, S.; Pergantisi, S. A. Anal. Chem. 2016, 88, 4909-4916.
- (4) Ermolin, M. S.; Fedotov, P. S. Rev. Anal. Chem 2016, 35, 185-199.
- (5) Benn, T. M.; Westerhoff, P. Environ. Sci. Technol. 2008, 42, 4133-4139.
- (6) Marbella, L. E.; Millstone, J. E. Chem. Mater. 2015, 27, 2721-
- (7) Cooke, P. M. Anal. Chem. 2000, 72, 169R-188R.
- (8) Huang, B.; Wang, W. Q.; Bates, M.; Zhuang, X. W. Science 2008, 319, 810-813.
- (9) von Diezmann, A.; Shechtman, Y.; Moerner, W. E. Chem. Rev. 2017, 117, 7244-7275.
- (10) Tan, Y. Z.; Jin, S.; Hamers, R. J. ACS Appl. Mater. Interfac. 2013, 5, 12975-12983.
- (11) Tvrdy, K.; Kamat, P. V. J. Phys. Chem. A 2009, 113, 3765-3772.
- (12) van Sark, W.; Frederix, P.; Van den Heuvel, D. J.; Gerritsen, H. C.; Bol, A. A.; van Lingen, J. N. J.; Donega, C. D.; Meijerink, A. J. Phys. Chem. B 2001, 105, 8281-8284.
- (13) Klyachkovskaya, E. V.; Vashchenko, S. V.; Stupak, A. P.; Gaponenko, S. V. J. Appl. Spectrosc. 2010, 77, 732-736.
- (14) Saurabh, S.; Perez, A. M.; Comerci, C. J.; Shapiro, L.; Moerner, W. E. J. Am. Chem. Soc. 2016, 138, 10398-10401.
- (15) Kolmakov, K.; Wurm, C. A.; Meineke, D. N. H.; Gottfert, F.; Boyarskiy, V. P.; Belov, V. N.; Hell, S. W. Chem. - Eur. J. 2014, 20, 146-157.
- (16) Resch-Genger, U.; Grabolle, M.; Cavaliere-Jaricot, S.; Nitschke, R.; Nann, T. Nat. Methods 2008, 5, 763-775.
- (17) Bu, X. B.; Chen, H. P.; Gai, H. W.; Yang, R. H.; Yeung, E. S. Anal. Chem. 2009, 81, 7507-7509.
  - (18) He, H.; Xie, C.; Ren, J. Anal. Chem. 2008, 80, 5951-5957.
- (19) Bandyopadhyay, S.; Peralta-Videa, J. R.; Gardea-
- Torresdey, J. L. Environ. Engr. Sci. 2013, 30, 118-125.
- (20) Hsiao, W. W. W.; Hui, Y. Y.; Tsai, P. C.; Chang, H. C. Acc. Chem. Res. 2016, 49, 400-407.
- (21) Wu, Y. Z.; Jelezko, F.; Plenio, M. B.; Weil, T. Angew. Chem. Int. Ed. 2016, 55, 6586-6598.
- (22) Reineck, P.; Francis, A.; Orth, A.; Lau, D. W. M.; Nixon-Luke, R. D. V.; Rastogi, I. D.; Razali, W. A. W.; Cordina, N. M.; Parker, L. M.; Sreenivasan, V. K. A.; Brown, L. J.; Gibson, B. C. Adv. Opt. Mat. 2016, 4, 1549-1557.
- (23) Pansare, V. J.; Hejazi, S.; Faenza, W. J.; Prud'homme, R. K. Chem. Mater. 2012, 24, 812-827.
- (24) Davies, G.; Hamer, M. F. Proc. R. Soc. London, Ser. A 1976, 348, 285-298.

- (25) Wang, X. Y.; Landis, E. C.; Franking, R.; Hamers, R. J. *Acc. Chem. Res.* **2010**, 43, 1205-1215.
- (26) Krueger, A.; Lang, D. *Adv. Funct. Mater.* **2012**, 22, 890-906.
- (27) Stavis, C.; Clare, T. L.; Butler, J. E.; Radadia, A. D.; Carr, R.; Zeng, H. J.; King, W. P.; Carlisle, J. A.; Aksimentiev, A.; Bashir, R.; Hamers, R. J. *Proc. Natl. Acad. Sci. U.S.A.* **2011**, *108*, 983-988.

(28) Chapman, R.; Plakhotnik, T. Opt. Lett. 2013, 38, 1847-1849.

- (29) Igarashi, R.; Yoshinari, Y.; Yokota, H.; Sugi, T.; Sugihara, F.; Ikeda, K.; Sumiya, H.; Tsuji, S.; Mori, I.; Tochio, H.; Harada, Y.; Shirakawa, M. *Nano Lett.* **2012**, *12*, 5726-5732.
  - (30) Gruber, A. Science 1997, 276, 2012-2014.
- (31) Singam, S. K. R.; Motylewski, J.; Monaco, A.; Gjorgievska, E.; Bourgeois, E.; Nesládek, M.; Giugliano, M.; Goovaerts, E. *Physical Review Applied* **2016**, *6*, 064013.
  - (32) Hegyi, A.; Yablonovitch, E. Nano Lett. 2013, 13, 1173-1178.
- (33) Sarkar, S. K.; Bumb, A.; Wu, X. F.; Sochacki, K. A.; Kellman, P.; Brechbiel, M. W.; Neuman, K. C. *Biomed. Opt. Express* **2014**, *5*, 1190-1202.
- (34) Balasubramanian, G.; Chan, I. Y.; Kolesov, R.; Al-Hmoud, M.; Tisler, J.; Shin, C.; Kim, C.; Wojcik, A.; Hemmer, P. R.; Krueger, A.; Hanke, T.; Leitenstorfer, A.; Bratschitsch, R.; Jelezko, F.; Wrachtrup, J. *Nature* **2008**, *455*, 648-651.
- (35) Taylor, J. M.; Cappellaro, P.; Childress, L.; Jiang, L.; Budker, D.; Hemmer, P. R.; Yacoby, A.; Walsworth, R.; Lukin, M. D. *Nat. Phys.* **2008**, *4*, 810-816.
- (36) Maze, J. R.; Stanwix, P. L.; Hodges, J. S.; Hong, S.; Taylor, J. M.; Cappellaro, P.; Jiang, L.; Dutt, M. V. G.; Togan, E.; Zibrov, A. S.; Yacoby, A.; Walsworth, R. L.; Lukin, M. D. *Nature* **2008**, 455, 644-647.
- (37) McGuinness, L. P.; Yan, Y.; Stacey, A.; Simpson, D. A.; Hall, L. T.; Maclaurin, D.; Prawer, S.; Mulvaney, P.; Wrachtrup, J.; Caruso, F.; Scholten, R. E.; Hollenberg, L. C. L. *Nat. Nanotechnol.* **2011**, *6*, 358-363.
- (38) Hall, L. T.; Cole, J. H.; Hill, C. D.; Hollenberg, L. C. L. *Phys. Rev. Lett.* **2009**, 103, 4.
- (39) Dolde, F.; Fedder, H.; Doherty, M. W.; Nobauer, T.; Rempp, F.; Balasubramanian, G.; Wolf, T.; Reinhard, F.; Hollenberg, L. C. L.; Jelezko, F.; Wrachtrup, J. *Nat. Phys.* **2011**, *7*, 450-463.
- (40) Grotz, B.; Beck, J.; Neumann, P.; Naydenov, B.; Reuter, R.; Reinhard, F.; Jelezko, F.; Wrachtrup, J.; Schweinfurth, D.; Sarkar, B.; Hemmer, P. *New J. Phys.* **2011**, *13*, 055004.
- (41) Toyli, D. M.; de las Casas, C. F.; Christle, D. J.; Dobrovitski, V. V.; Awschalom, D. D. *Proc. Natl. Acad. Sci. U.S.A.* **2013**, *110*, 8417-8421.
- (42) Levchenko, A. O.; Vasil'ev, V. V.; Zibrov, S. A.; Zibrov, A. S.; Sivak, A. V.; Fedotov, I. V. Appl. Phys. Lett. **2015**, 106, 102402.
- (43) Kaviani, M.; Deák, P.; Aradi, B.; Frauenheim, T.; Chou, J.-P.; Gali, A. *Nano Lett.* **2014**, *14*, 4772-4777.
  - (44) Cui, S.; Hu, E. L. Appl. Phys. Lett. 2013, 103, 051603.
- (45) Hauf, M. V.; Grotz, B.; Naydenov, B.; Dankerl, M.; Pezzagna, S.; Meijer, J.; Jelezko, F.; Wrachtrup, J.; Stutzmann, M.; Reinhard, F.; Garrido, J. A. *Phys. Rev. B* **2011**, *8*3.
- (46) Maier, F.; Riedel, M.; Mantel, B.; Ristein, J.; Ley, L. *Phys. Rev. Lett.* **2000**, *85*, 3472-3475.
- (47) Grotz, B.; Hauf, M. V.; Dankerl, M.; Naydenov, B.; Pezzagna, S.; Meijer, J.; Jelezko, F.; Wrachtrup, J.; Stutzmann, M.; Reinhard, F.; Garrido, J. A. *Nat. Comm.* **2012**, 3.
- (48) Ohashi, K.; Rosskopf, T.; Watanabe, H.; Loretz, M.; Tao, Y.; Hauert, R.; Tomizawa, S.; Ishikawa, T.; Ishi-Hayase, J.; Shikata, S.; Degen, C. L.; Itoh, K. M. *Nano Lett.* **2013**, *13*, 4733-4738.
- (49) Zvyagin, A. V.; Manson, N. B. In *Ultrananocrystalline Diamond*, Shenderova, O. A.; Gruen, D. M., Eds.; Elsevier: New York, 2012, pp 327-354.

- (50) Santori, C.; Barclay, P. E.; Fu, K.-M. C.; Beausoleil, R. G. *Phys. Rev. B* **2009**, 79.
- (51) Chung, P. H.; Perevedentseva, E.; Cheng, C. L. Surf. Sci. **2007**, 601, 3866-3870.
- (52) Shames, A. I.; Osipov, V. Y.; Boudou, J. P.; Panich, A. M.; von Bardeleben, H. J.; Treussart, F.; Vul', A. Y. *J. Phys. D: Appl. Phys.* **2015**, *48*, 155302.
- (53) Osipov, V. Y.; Shames, A. I.; Enoki, T.; Takai, K.; Baidakova, M. V.; Vul, A. Y. *Diamond Relat. Mater.* **2007**, *16*, 2035-2038.
- (54) Horowitz, V. R.; Aleman, B. J.; Christle, D. J.; Cleland, A. N.; Awschalom, D. D. *Proc Natl Acad Sci U.S.A.* **2012**, *109*, 13493-13497.
- (55) Robledo, L.; Bernien, H.; Sar, T. v. d.; Hanson, R. *New J. Phys.* **2011**, *13*, 025013.
- (56) Popa, J.; Gaebel, T.; Neumann, P.; Jelezko, F.; Wrachtrup, J. Isr. J. Chem. **2006**, *46*, 393-398.

### Table-of-contents figure

